Letters

Enhanced Axial Misalignment Tolerance in a 10-kW Autonomous Underwater Vehicle Wireless Charging System Utilizing a Split Solenoid Coupler

Amr Mostafa, *Student Member, IEEE*, Yao Wang, Fei Lu, and Hua Zhang, *Member, IEEE*

***Abstract*—This letter presents a 10-kW wireless charging system for autonomous underwater vehicles, utilizing a split solenoid coupler to enhance axial misalignment tolerance. Comparative finite-element analysis with traditional solenoid structures indicates the split solenoid design's superiority in reducing inductance fluctuations, with a 22% reduction in coupling coefficient fluctuation and a 24.8% and 25.6% reduction in self-inductance and mutual inductance fluctuations, respectively, at an 80-mm axial misalignment. Experimental validation of the system demonstrates high efficiency in saltwater environments, achieving a peak efficiency of 96.3% at 7.1 kW and a maximum power output of 10.6 kW at 95.6% efficiency. A tight coupling coefficient of 0.69 along with the split solenoid coupler improves both axial misalignment and system efficiency enabling high-power wireless power transfer in marine environments.**

***Index Terms*—Autonomous underwater vehicles (AUVs), inductive power transfer (IPT), wireless charging.**

I. Introduction

AUTONOMOUS underwater vehicles (AUVs) are increasingly used in oceanography and underwater exploration, with inductive power transfer (IPT) offering a reliable high-power charging solution [1], [2], [3], [4], [5], [6], [7]. However, the marine environment presents unique challenges for IPT systems, particularly due to the conductivity of seawater, which can lead to increased losses and reduced system efficiency [8]. Axial misalignment in IPT systems remains a challenge [4], [6], [7], [9], [10].

Axial misalignment occurs when the AUVs' receiving coil is not aligned with the transmitting coil in the docking station along their shared central axis, as shown in Fig. 1. This can happen when the AUV is inserted too far or not far enough into the docking station, causing the receiving coil to be displaced from the optimal charging position. This misalignment is a common challenge in AUV charging due to the difficulty in achieving perfect alignment between the vehicle and the charging station in marine environments.

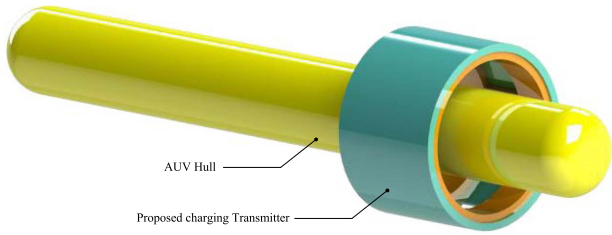

Fig. 1. Conceptual structure of a hull-compatible IPT system.

In [11], a traditional solenoid coupler structure is utilized for an underwater simultaneous wireless power and data transfer system. While this structure demonstrates good performance, it is still susceptible to power fluctuations under axial misalignment conditions. In contrast, we propose a novel split solenoid coupler structure that consists of four smaller solenoids: two for the transmitter and two for the receiver, with a gap between them. This split arrangement reduces the impact of axial misalignment on the coupling coefficient and self-inductances, leading to enhanced misalignment tolerance and improved power transfer stability compared to the traditional solenoid structure in [11]. Finally, the high power transfer capability and efficiency of the split solenoid structure are experimentally validated through a 10-kW IPT prototype in saltwater, demonstrating its practical feasibility and performance in challenging marine environments.

The rest of this letter is organized as follows. Section II provides a detailed description of the split solenoid structure. Section III presents the experimental setup and results, demonstrating an improved axial misalignment performance. Finally, Section IV concludes this letter, summarizing key contributions.

II. Split Solenoid Magnetic Coupler

A. Coupler Structure Overview

Fig. 1 shows the proposed design concept of a hull-compatible inductive charger for AUVs. The transmitter (L_1) and the

Manuscript received 9 April 2024; revised 11 May 2024 and 19 June 2024; accepted 7 July 2024. Date of publication 19 July 2024; date of current version 4 September 2024. This work was supported by the National Science Foundation under Grant 2301637. *(Corresponding author: Hua Zhang.)*

Amr Mostafa is with Tesla Inc., Palo Alto, CA 94304 USA (e-mail: amrmostafa@tesla.com).

Yao Wang is with the School of Electrical and Electronic Engineering, Nanyang Technological University, Singapore 639798 (e-mail: yao.wang@ntu.edu.sg).

Fei Lu and Hua Zhang are with the Department of Electrical and Computer Engineering, Lehigh University, Bethlehem, PA 18015 USA (e-mail: fel324@lehigh.edu; huz524@lehigh.edu).

Color versions of one or more figures in this article are available at https://doi.org/10.1109/TPEL.2024.3431285.

Digital Object Identifier 10.1109/TPEL.2024.3431285

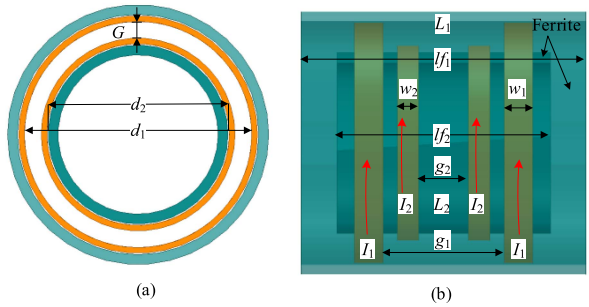

Fig. 2. Proposed split solenoid magnetic coupler structure, showing the details and different viewing angles. (a) Side view of the coupler. (b) Front view of the coupler.

TABLE I
MAGNETIC COUPLER DIMENSION PARAMETERS

l_{f1} (l_{f2})	L_1 (L_2) ferrite length	w_1 (w_2)	L_1 (L_2) winding width
d_1(d_2)	L_1 (L_2) inner diameter	g_1(g_2)	L_1 (L_2) split gap distance
G	Water gap distance	D	Axial misalignment

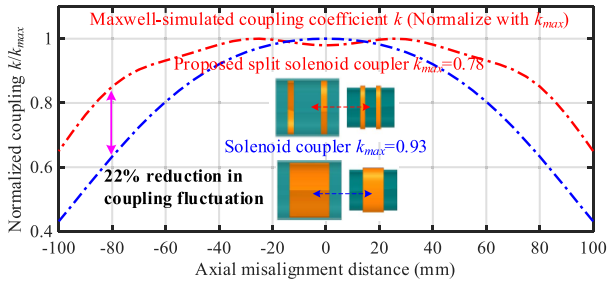

Fig. 3. Maxwell-simulated normalized coupling k at axial misalignment.

receiver (L_2) are each constructed of two series-connected solenoid coils [see Fig. 2(a) and (b)]. The gap g_1 is crucial to axial misalignment performance. Structural dimensions are in Table I. The coupler's diameter (d_1 and d_2) shown in the side view [see Fig. 2(a)] can adapt to AUV size, with transfer distance defined as G. Inner and outer ferrite rings in Fig. 2(b) are critical to minimize magnetic leakage.

B. Comparison to the Solenoid Structure

Finite-element analysis (FEA) is utilized to examine how gap spacing in a split solenoid structure can enhance axial misalignment tolerance. The tradeoff of this improvement is a marginal decrease in the coupling coefficient when the coils are perfectly aligned.

Fig. 3 compares the split solenoid structure with a traditional solenoid, revealing a 22% reduction in coupling coefficient fluctuation at 80-mm axial misalignment. In addition, the proposed coupler exhibits 24.8% less fluctuation in the primary self-inductance (L_1) and 25.6% less fluctuation in the mutual inductance (L_M) at an axial misalignment of 80 mm compared with the conventional coupler, which exhibits a similar trend to the coupling coefficient shown in Fig. 3. The secondary self-inductance (L_2) shows similar fluctuations for both the

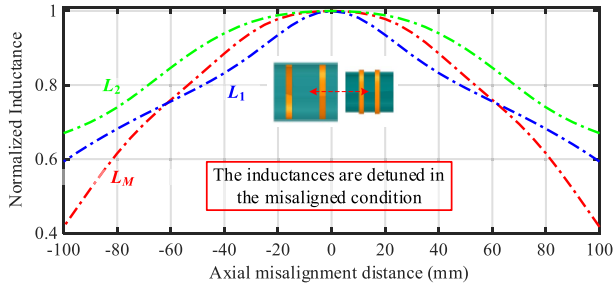

Fig. 4. Maxwell-simulated normalized mutual inductance L_M and self-inductances L_1 and L_2, showing detuning at axial misalignment.

coupler designs, with no significant difference (0%) observed at an axial misalignment of 80 mm.

Fig. 4 displays the normalized inductances under axial misalignment, highlighting a significant detuning effect that can impact power transfer efficiency. In AUV applications, where tight coupling is necessary to minimize seawater losses, self-inductance detuning is exacerbated by close transmission distances and large misalignments. The commonly used cylindrical coupler structures in AUVs are particularly susceptible to self-inductance fluctuations due to their geometry, making misalignment tolerant systems difficult to achieve.

C. Effect of Self-Inductance Detuning on Output Current

In Fig. 11, this letter selects the series–series topology for simplicity. In the well-aligned case, the resonance is expressed as follows:

$$\omega_0 = 1/\sqrt{L_{1,0}C_1} = 1/\sqrt{L_{2,0}C_2}. \tag{1}$$

Mutual inductance and equivalent resistance are defined as

$$L_M = k\sqrt{L_1 L_2}, \quad R_{Le} = 8/\pi^2 \times R_L. \tag{2}$$

To analyze detuning, the changes in self-inductances relative to resonance values $L_{1,0}$ and $L_{2,0}$ are defined as follows:

$$\Delta\gamma_1 = (L_{1,0} - L_1)/L_{1,0}, \quad \Delta\gamma_2 = (L_{2,0} - L_2)/L_{2,0}. \tag{3}$$

The first harmonic approximation for output current at resonance is further derived as follows:

$$\begin{bmatrix} V_1 \\ 0 \end{bmatrix} = \begin{bmatrix} j\omega_0 L_{1,0}(-\Delta\gamma_1) & j\omega_0 L_M \\ j\omega_0 L_M & R_{Le} + j\omega_0 L_{2,0}(-\Delta\gamma_2) \end{bmatrix} \begin{bmatrix} I_1 \\ I_2 \end{bmatrix}. \tag{4}$$

From (4), solving for I_2 yields

$$I_2 = V_1 L_M / \left(j\omega_0 {L_M}^2 - j\omega_0 L_{1,0} L_{2,0} \Delta\gamma_1 \Delta\gamma_2 + L_{1,0} R_{Le} \Delta\gamma_1\right). \tag{5}$$

To simplify the analysis, I_2 can be rewritten as follows:

$$I_2 = V_1/(j\omega_0 L_M) \cdot \alpha \tag{6}$$

where α is a power scaling factor resulting from self-inductance detuning. If there is no self-inductance detuning, $\alpha = 1$. From

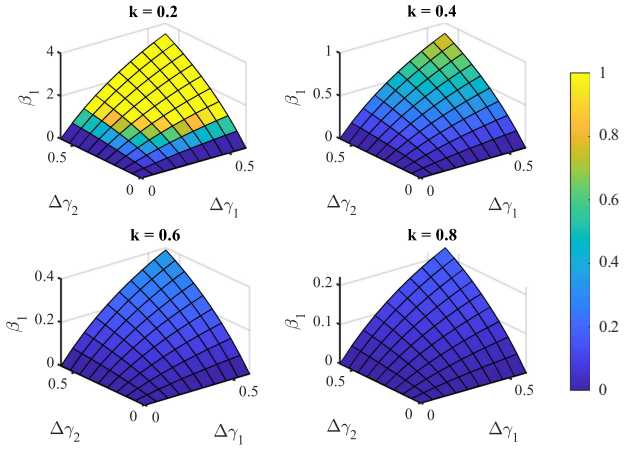

Fig. 5. Calculated β_1 at different coupling coefficient k, considering the detuning parameters $\Delta\gamma_1$ and $\Delta\gamma_2$ of the self-inductances.

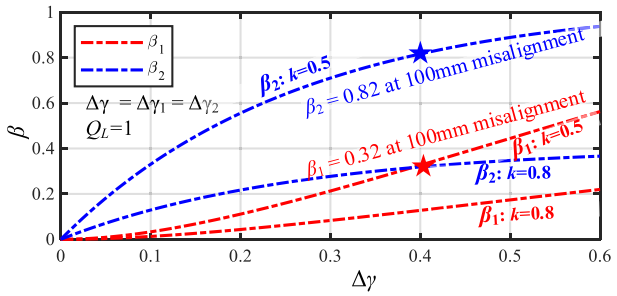

Fig. 6. Calculated β_1 and β_2 at different detuning factor $\Delta\gamma$ and coupling coefficient k, assuming $\Delta\gamma = \Delta\gamma_1 = \Delta\gamma_2$.

(2), (3), and (5), α is derived as follows:

$$\alpha = \frac{1}{(1-\beta_1) - j\beta_2} \tag{7}$$

where two parameters β_1 and β_2 are defined as

$$\begin{cases} \beta_1 = \frac{1}{k^2} \cdot \frac{\Delta\gamma_1}{1+\Delta\gamma_1} \cdot \frac{\Delta\gamma_2}{1+\Delta\gamma_2} \\ \beta_2 = \frac{1}{k^2} \cdot \frac{\Delta\gamma_1}{1+\Delta\gamma_1} \cdot \frac{1/Q_L}{1+\Delta\gamma_2}. \end{cases} \tag{8}$$

The load quality factor is defined as $Q_L = \omega_0 L_{2,0}/R_{Le}$. In a tightly coupled IPT system, $Q_L \approx 1$ for load matching. Based on FEA simulation in Section II-B, $\Delta\gamma_1$ and $\Delta\gamma_2$ are in the range of [0, 0.6] for the proposed coupler, resulting in $\beta_1 < \beta_2$.

Fig. 5 shows the effect of $\Delta\gamma_1$ and $\Delta\gamma_2$ according to (8). It illustrates the parameter β_1 at different coupling coefficient k. When $k = 0.2$, the maximum $\beta_1 = 3.5$; when $k = 0.8$, the maximum $\beta_1 = 0.32$, showing that a strong coupling coefficient reduces the variation range of β_1.

Fig. 6 further shows the effect of inductance detuning on β_1 and β_2. Since L_1 and L_2 have similar detuning characteristics (from Fig. 4), the inductance variation is set as $\Delta\gamma = \Delta\gamma_1 = \Delta\gamma_2$ for simplicity. The magnitudes of β_1 and β_2 both positively correlate with k. The blue and red stars show the approximate values of β_1 and β_2, respectively, at 100-mm axial misalignment.

Fig. 7 shows the variation in the magnitude of the scaling factor $|\alpha|$. In a tightly coupled system ($k = 0.8$), the inductance detuning results in increased output current based on (6) and

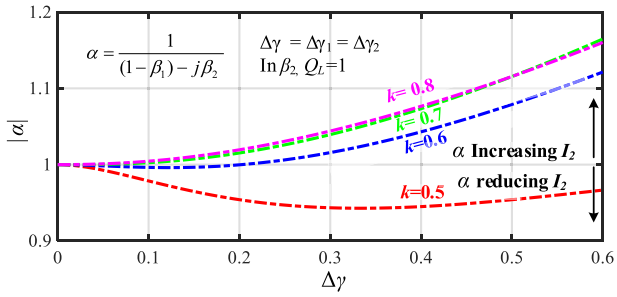

Fig. 7. Calculated magnitude of the power scaling factor $|\alpha|$ at detuning factor $\Delta\gamma$ and coupling coefficient k, assuming $\Delta\gamma = \Delta\gamma_1 = \Delta\gamma_2$.

TABLE II
IMPLEMENTED MAGNETIC COUPLER DIMENSIONS

l_{f1}	200 mm	l_{f2}	150 mm
w_1	23 mm	w_2	12 mm
d_1	160 mm	d_2	140 mm
g_1	90 mm	g_2	40 mm
G	10 mm	D	0–80 mm

consequently power. However, when $k = 0.5$, the scaling factor $|\alpha|$ contributes to reducing power. It is important to note that the detuning does not result in a reduced overall current since L_M is also reduced in (6).

In the aforementioned analysis, the assumption is made that the system operates at resonance when perfectly aligned. However, in practical operation, many designs necessitate a detuning of compensation capacitors to achieve zero-voltage switching (ZVS). To consider capacitor detuning, recalculate $L_{1,0}$ and $L_{2,0}$ by rewriting (1) as follows:

$$L_{1,0} = 1/\left(\omega_0{}^2 C_{1,\text{detuned}}\right), \quad L_{2,0} = 1/\left(\omega_0{}^2 C_{2,\text{detuned}}\right). \tag{9}$$

To summarize the design process, (3) can be used to recalculate $\Delta\gamma_1$ and $\Delta\gamma_2$ for each position including a well-aligned case, resulting in (6) that considers both capacitor and self-inductance detuning.

D. Split Unipolar Coupler Implementation

Table II details the split solenoid coupler's structure parameters. The transmitter coil L_1 and the receiver coil L_2 have ferrite lengths of 200 and 150 mm, respectively, extending beyond the coil to shield AUV electronics and minimize seawater leakage losses.

The magnetic coupler is shown in Fig. 8. The primary coil comprises nine turns, while the secondary has five turns. High per turn inductance necessitates half-turns for construction, with each split part of the transmitter having 4.5 turns on opposite sides to maintain symmetry.

Fig. 9 illustrates mutual and self-inductances at various misalignments. At 80-mm misalignment, L_1 and L_2 decrease by 31.6% and 25%, respectively, and L_M by 38.5%, aligning with FEA results shown in Fig. 4.

The proposed split solenoid coupler is designed for seamless integration within the fiberglass hull of an AUV, providing

Fig. 8. Prototype of coupler structure. (a) Fully assembled coupler. (b) Bare windings of transmitter. (c) Assembled reciever.

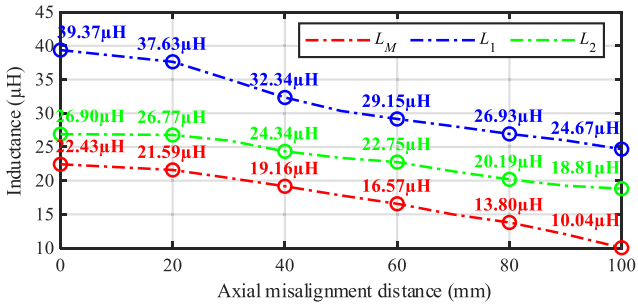

Fig. 9. Measured self- and mutual inductances at misalignment positions.

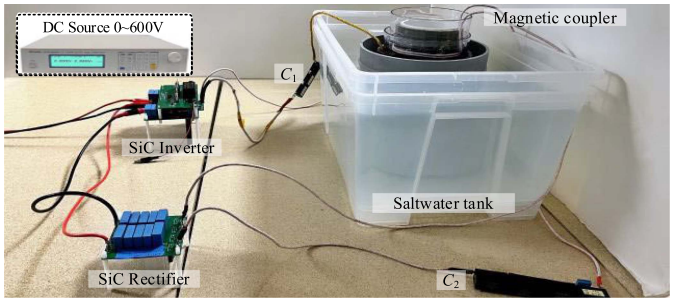

Fig. 10. Implemented IPT prototype under the saltwater testing condition.

inherent protection against the conductive seawater environment. The hollow receiver coil design allows for the efficient placement of AUV components, such as batteries or electronic modules, within the coupler structure. These properties facilitate the integration of the wireless charging system into the existing AUV architectures while minimizing the impact on the vehicle's size and weight.

III. Experimental Validation

A. 10-kW Prototype Power-Circulating Testing

Fig. 10 illustrates the saltwater test bench. The power recirculation setup, as shown in Fig. 11, is an arrangement where the rectified dc output of the wireless power transfer system is connected back to the dc input, creating a closed loop for power circulation. This configuration allows the system to effectively serve as its own load, as discussed in [12]. The main advantage

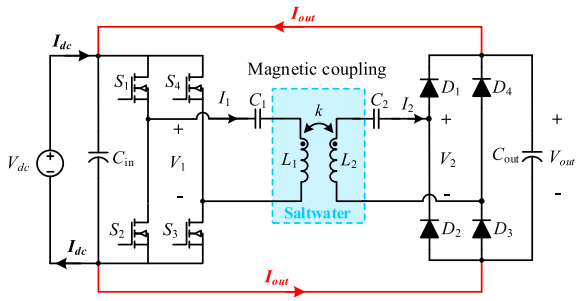

Fig. 11. Equivalent circuit of the implemented power-circulating testing bench.

TABLE III
Specifications of the Implemented IPT System in the Well-Aligned Case

Input V_{DC}	100–500 V	Output V_{out}	100–500 V
Inverter MOSFET	C3M0120100K	Rectifier diode	C4D20120D
Water conductivity	56.7 mS	Water salinity	35‰
Frequency f	200 kHz	k (aligned)	0.69
L_1 (aligned)	39.37 μH	L_2 (aligned)	26.9 μH
C_1	22.92 nF	C_2	25.51 nF

of this approach is that the dc input source only needs to provide the power required to offset system losses, enabling high power testing capability with a lower power demand on the dc source. In this setup, the system behaves as a constant voltage load, continuously recycling the same power. The voltage and current loads observed across all the system components are consistent with those seen in a system operating under a full power dc source.

System parameters are given in Table III. Tests were conducted with dc voltages between 100 and 550 V, using a 200-kHz inverter. The magnetic coupler, made from 800-strand 0.1-mm Litz wire, has a coupling coefficient k of 0.69 at a 10-mm transfer distance. It was submerged in 34.9‰ salinity water, with conductivity at 56.7 mS/cm and temperature at 22.4 °C. To manage thermal loads, heat sinks and cooling fans were used. The SiC MOSFETs (C3M0120100K) operate within their continuous current ratings. The rectifier design employs C4D20120D SiC diodes, which are rated for 1200 V and 20-A continuous current. Each diode package contains two diodes, which are connected in parallel, with four packages used for the full-bridge rectifier.

B. Well-Aligned Power Transfer Capability

Fig. 12 displays waveforms at zero-phase-angle operation with matched input and output voltages $V_{\mathrm{DC}} = V_{\mathrm{out}} = 550$ V, yielding 8.63-kW output power and 96.27% efficiency in saltwater. Fig. 13 indicates that within a $V_{\mathrm{DC}} = V_{\mathrm{out}} = 100$–$550$ V range, power spans 0.28–8.63 kW. Peak efficiencies are 96.99% at 5.13 kW in air and 96.29% at 7.14 kW in saltwater, 0.7% discrepancy due to saltwater's ion-induced eddy current losses.

C. Axial Misaligned Power Transfer Performance

Fig. 14 demonstrates how axial misalignment affects output power at various input voltages. A 50-mm misalignment results

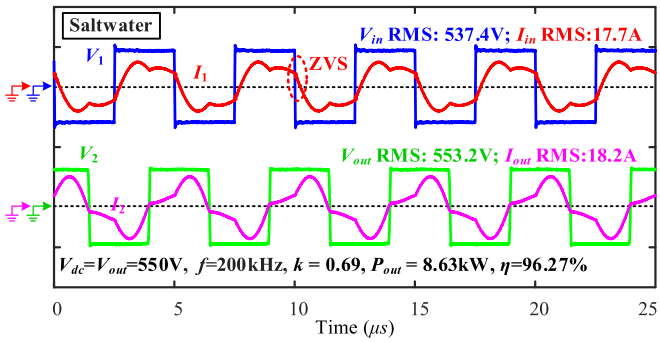

Fig. 12. Experimental waveforms in saltwater at the well-aligned position with $k = 0.69$, $V_{\mathrm{DC}} = V_{\mathrm{out}} = 550$ V, and $P_{\mathrm{out}} = 8.63$ kW.

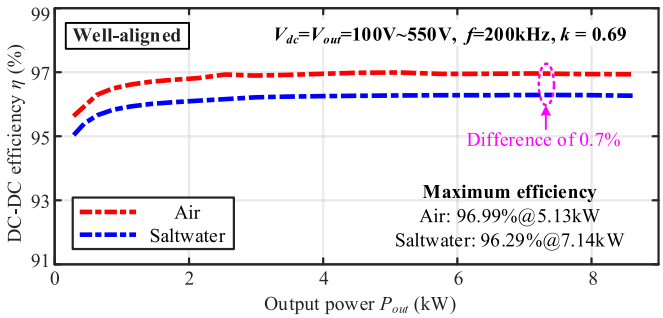

Fig. 13. Experimental output power and DC–DC efficiency at the well-aligned position, comparing the performance in the air and saltwater conditions.

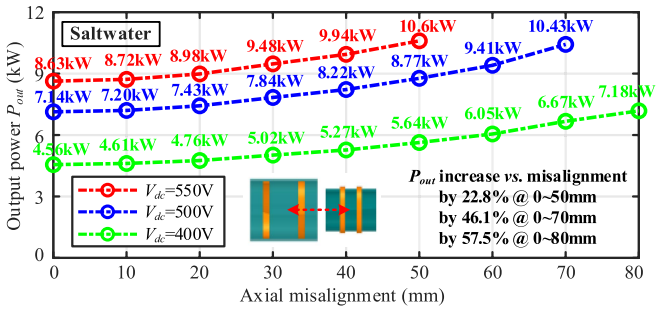

Fig. 14. Experimental output power at misalignment in saltwater environment.

in a 22.8% power increase. At 70 and 80 mm, power fluctuation reaches 46.1% and 57.5%, respectively.

Fig. 15 presents efficiency under misalignment. At 80 mm, efficiency drops by 1.31% in air and 4.9% in saltwater, with the efficiency gap between the two widening from 0.7% to 4.28%. In addition, it details the power loss distribution in saltwater at 0-mm misalignment with an input voltage of 550 V and an output power of 8.63 kW.

Fig. 14 demonstrates how axial misalignment affects output power at various input voltages. At an input voltage of 550 V and an axial misalignment of 50 mm, the system achieves a peak output power of 10.6 kW, highlighting its high power transfer capability under misalignment conditions. As shown in Fig. 15, high power transfer is maintained with a small efficiency drop from 96.27% to 95.72%, demonstrating system robustness to axial misalignment.

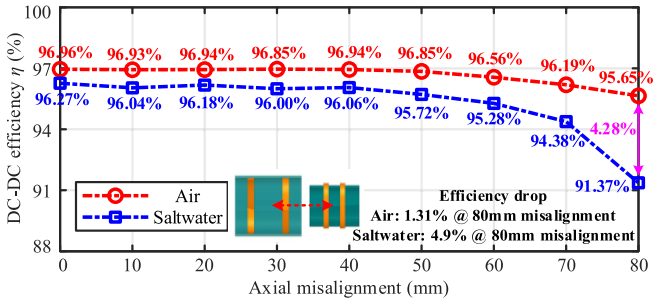

Fig. 15. Experimental DC–DC efficiency at misalignment in the air and saltwater environments, showing that the misalignment can cause efficiency drop in saltwater.

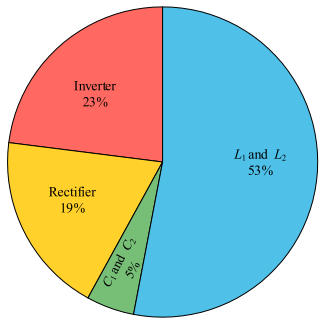

Fig. 16. Power loss distribution of components at well aligned 8.63 kW in seawater. The L_1 and L_2 loss includes both the conduction/magnetic loss in the coupler and the eddy current loss in the seawater environment.

D. Power Loss Analysis

In the power circulating setup, the input voltage V_{DC} equals the output voltage V_{out}. At the steady state, the input power from the dc source represents the total system losses. To measure system efficiency, a Chroma 62024P dc power supply provided input power, with voltage measurements validated by a Keithley DMM6500 multimeter. Output current was measured using a Tektronix TCP0030A current probe and a Tektronix 5 Series oscilloscope. Since the power loss is measured independently of the output current, any error in the current probe accuracy will have a minimal effect on the calculated efficiency.

Fig. 16 presents a breakdown of the power losses in each component when operating in saltwater with a well-aligned coupler, at an input and output voltage of 550 V, a switching frequency of 200 kHz, and an output power level of 8.6 kW. The figure reveals that the main losses occur in the magnetic coupler (L_1 and L_2), accounting for 53% of the total losses. The inverter contributes to 23% of the losses, followed by the rectifier at 19% and the capacitors (C_1 and C_2) at 5%.

IV. Conclusion

This letter presents a split solenoid coupler structure to improve axial misalignment tolerance for AUVs without compromising rotational performance compared to a traditional solenoid structure. A 10-kW IPT prototype is implemented in saltwater, achieving a peak power level of 10.6 kW with efficiency of 95.6% and a peak efficiency of 96.3% at 7.1 kW. Besides, the experimental results show that the proposed coupler only has 0.7% efficiency difference in saltwater compared to the air condition at a well-aligned position.

REFERENCES

[1] C. Cai, S. Wu, Z. Zhang, L. Jiang, and S. Yang, "Development of a fit-to-surface and lightweight magnetic coupler for autonomous underwater vehicle wireless charging systems," *IEEE Trans. Power Electron.*, vol. 36, no. 9, pp. 9927–9940, Sep. 2021.

[2] S. Wu, C. Cai, A. Wang, Z. Qin, and S. Yang, "Design and implementation of a uniform power and stable efficiency wireless charging system for autonomous underwater vehicles," *IEEE Trans. Ind. Electron.*, vol. 70, no. 6, pp. 5674–5684, Jun. 2023.

[3] A. Mostafa, Y. Wang, H. Zhang, S. Tangirala, and F. Lu, "An ultra-fast wireless charging system with a hull-compatible coil structure for autonomous underwater vehicles (AUVs)," in *Proc. IEEE Transp. Electrific. Conf. Expo*, 2022, pp. 279–284.

[4] Z. Cheng, Y. Lei, K. Song, and C. Zhu, "Design and loss analysis of loosely coupled transformer for an underwater high-power inductive power transfer system," *IEEE Trans. Magn.*, vol. 51, no. 7, Jul. 2015, Art. no. 8401110.

[5] C. R. Teeneti, T. T. Truscott, D. N. Beal, and Z. Pantic, "Review of wireless charging systems for autonomous underwater vehicles," *IEEE J. Ocean. Eng.*, vol. 46, no. 1, pp. 68–87, Jan. 2021.

[6] Z. Yan et al., "Free-rotation wireless power transfer system based on composite anti-misalignment method for AUVs," *IEEE Trans. Power Electron.*, vol. 38, no. 4, pp. 4262–4266, Apr. 2023.

[7] Y. Zeng, C. Lu, R. Liu, X. He, C. Rong, and M. Liu, "Wireless power and data transfer system using multidirectional magnetic coupler for swarm AUVs," *IEEE Trans. Power Electron.*, vol. 38, no. 2, pp. 1440–1444, Feb. 2023.

[8] Y. Wang, A. Mostafa, Z. Zheng, H. Zhang, C. Zhu, and F. Lu, "Experimental investigation of the eddy-current and dielectric loss of underwater IPT system," in *Proc. IEEE Energy Convers. Congr. Expo.*, 2023, pp. 6371–6375.

[9] T. Kan, Y. Zhang, Z. Yan, P. P. Mercier, and C. C. Mi, "A rotation-resilient wireless charging system for lightweight autonomous underwater vehicles," *IEEE Trans. Veh. Technol.*, vol. 67, no. 8, pp. 6935–6942, Aug. 2018.

[10] T. Li, Z. Sun, Y. Wang, J. Mai, and D. Xu, "Undersea simultaneous wireless power and data transfer system with extended communication distance and high rate," *IEEE Trans. Power Electron.*, vol. 39, no. 3, pp. 2917–2921, Mar. 2024.

[11] Y. Wang, T. Li, M. Zeng, J. Mai, P. Gu, and D. Xu, "An underwater simultaneous wireless power and data transfer system for AUV with high-rate full-duplex communication," *IEEE Trans. Power Electron.*, vol. 38, no. 1, pp. 619–633, Jan. 2023.

[12] S. Lu, D. Kong, S. Xu, L. Luo, and S. Li, "A high-efficiency 80-kW split planar transformer for medium-voltage modular power conversion," *IEEE Trans. Power Electron.*, vol. 37, no. 8, pp. 8762–8766, Aug. 2022.